
Article:
Kerridge, G., Sinclair, D.C. orcid.org/0000-0002-8031-7678 and Dean, J.S. orcid.org/0000-0001-7234-1822 (2021) Resource efficient exploration of ternary phase space to develop multi-layer ceramic capacitors. Acta Materialia, 207. 116690. ISSN 1359-6454

https://doi.org/10.1016/j.actamat.2021.116690

Resource Efficient Exploration of Ternary Phase Space to Develop Multi-Layer Ceramic Capacitors

G. Kerridge, D. C. Sinclair and J. S. Dean
Department of Materials Science & Engineering, Sir Robert Hadfield Building, University of Sheffield, Mappin Street, UK, S1 3JD.

Abstract

We demonstrate a fast, efficient combinatorial method for the optimisation of materials for multi-layer ceramic capacitors (MLCCs). Experimentally gathered permittivity-temperature profiles for nine compositions spanning a solid solution are used as input, and with series mixing rules, binary and ternary permittivity contour maps are calculated based on individual layer thicknesses. These are converted into Temperature Coefficient of Capacitance (TCC) contour maps and an algorithm is then used to identify material combinations and individual thicknesses suitable for various MLCC classifications. These facilitate targeted experimentation and allowed experimental verification of the methodology. The approach highlights that binary systems can achieve X9(U, T, S and R) classification but the addition of a third complimentary material can facilitate a tighter TCC classification (X9P) with a wider tolerance in layer thicknesses, providing a better strategy for mass production of MLCCs. The room temperature permittivity (ε_{RT}) for combinations with similar TCC values can also be evaluated to ensure adequate ε_{RT} is achieved for commercial applications.

Introduction

Multi-layer ceramic capacitors (MLCCs) based on ferroelectric $BaTiO_3$ (BT) are one of the most heavily produced passive components in electronic circuitry and have been a workhorse of the electronic components industry for more than 30 years [1]. The global MLCC market generated ~3.6 trillion $BaTiO_3$-based units last year was valued at USD 5,6 billion in 2018. Until the advent of COVID 2019, the MLCC market was expected to reach USD 8.0 billion by the end of 2024 with a compound annual growth rate of 6.38% [2]. MLCCs are relied upon and used across multiple industries with significant demands coming from automotive and telecommunications, causing global supply shortage issues in 2018. An example of this is the recent iPhone X which requires over 1000 MLCCs compared to its predecessor the iphone 6S with 700 pieces [3]. Another significant growth industry for MLCCs is the automotive sector due to the drive towards ‘under-the-hood’ electronics and increasing production of electric vehicles, where a modern Tesla car requires over 10 times more MLCCs than a modern mobile phone [3]. These applications require MLCCs to operate at higher temperature and/or voltages to increase the driving range and charge/discharge times, thus requiring improvements in the temperature stability of the permittivity and/or dielectric breakdown of the ceramics.

To increase the capacitance of an MLCC, the material is required to possess a large permittivity or be fabricated with thinner layers and/or larger area. If the thickness of the dielectric layer is decreased, it brings not only manufacturing challenges but

performance and reliability issues due to the increased electric field across the material. Increasing the area is also limited due to the physical case size of the device. By stacking thin layers of BT-based dielectric ceramics (ca 1 – 10 microns) between base metal electrodes (e.g. Ni), MLCCs can possess high capacitance with a temperature stability designed to be retained over designated temperature ranges. Ferroelectric BT is typically the base material as it possesses a high permittivity ~ 1000 - 2500 at room temperature, rising to a sharp maximum of ~ 12,000 at the Curie Temperature, T_c of ~ 120 ºC; however, modification to the heavily temperature dependent permittivity through chemical doping is required to meet industrial requirements and specifications [4, 5]. This temperature stability is measured by a metric known as the Temperature Coefficient of Capacitance (TCC) which describes the maximum percentage change in capacitance over a specified temperature range using a reference room temperature of 25°C and calculated as:

$$TCC(T) = 100 \times \frac{\varepsilon_T - \varepsilon_{RT}}{\varepsilon_{RT}}$$

Equation 1.

where ε_T is the permittivity at a temperature T, and ε_{RT} is the reference permittivity at a room temperature of 25º C. Using a specified temperature range and TCC fluctuation, capacitors can be subdivided into categories using a letter-number-letter code. A selection of these codes is provided in Table 1. For example, a ± 15% temperature variation in TCC across a temperature window of -55 to +125 ºC is known as X7R. TCC changes can also be asymmetric, such as Z5U, which allows TCC changes of +22 to -56% over a temperature from +10 to +85 ºC.

Low temperature code (ºC)	High temperature code (ºC)	Allowed capacitance change (TCC, %)
X = −55	4 = +65	P = ±10
Y = −30	5 = +85	R = ±15
Z = +10	6 = +105	S = ±22
	7 = +125	T = +22/−33
	8 = +150	U = +22/−56
	9 = +200	V = +22/−82

Table 1 A list of class II capacitor codes that provides the operational temperature window and allowed changes in TCC.

The overall permittivity-temperature (ε-T) profile depends on many parameters, including but not limited to; BT grain size, B/T ratio, dopant concentration(s)/distribution(s), volume fraction of grain core and shell regions, thickness of the dielectric layers and the applied electric field [6-17]. Through an intensive trial and error process, various ceramic formulations [18] and device processing conditions (i.e. milling, heating/cooling rates, oxygen partial pressure(s), sintering temperatures and dwell times) [19, 20] are employed to create different volume fractions of core and shell regions to systematically modify the ε-T profile of BT-based ceramics. TCC can thus be controlled over a sufficiently wide temperature range to satisfy industrial standards *via* optimisation of appropriate core-shell volume fractions [10, 21].

It can take several years to develop and optimise a formulation to meet the required TCC. Unfortunately, many fail on other device requirements, such as the Voltage Coefficient of Capacitance (VCC), Electric field Breakdown Strength (EBS), Fatigue Resistance (Life-Time), dielectric loss (tan δ) or resistivity (RC constant). As such very few formulations succeed to commercial applications. Typically, this is done by using a traditional solid-state route. Powder processes such as selecting and drying reagents, calcination and sintering uses substantial energy and time for each step. Techniques such as Finite Element Modelling (FEM) have made it possible to simulate the permittivity response of core-shell microstructured ceramics (on the basis the shell is more resistive than the core) [22-24] and can provide insight and guidance into experimentation of the desired volume fractions of core and shell materials in the dielectric [25], the effects of electrode roughness [26] and the grain size effect on the electric field dependence of the permittivity [27].

Typically for BT-based MLCCs, the dielectric requires $\varepsilon_{RT} > 1000$. There have been investigations on other variations in the layering of materials to alter the way they combine their electrical properties. Instead of single-layer parallel combinations, bi-layer combinations of different materials in direct contact have also been investigated. Amaral et al [28] combined undoped $BaTiO_3$ and $BaTi_{1-x}Zr_xO_3$, where x = 0.05 to 0.15. As the difference in Zr-content increased between adjacent layers, the permittivity profiles deviated from the prediction based on the ε-T profiles of the two individual materials. SEM results revealed Zr-diffusion at the interface where the Zr-content was intermediate between x = 0.00 and 0.15 of the respective layers. Consequently, the ε-T profile of the interface was not included in the model, leading to a disparity between the measured and calculated ε-T profiles.

Following the same concept, Song et al. [29] selected their materials to limit diffusion between the layers. The materials chosen were a series of $0.975BaTi_{1-x}Sn_xO_3$-$0.025Ba(Cu_{1/3}Nb_{2/3})O_3$, with the Sn doping level increasing in uniform steps from x = 0.01 to 0.08. The layers were separated by Pt electrodes and stacked in the MLCC to ensure the chemical composition difference between any layer and its neighbour was $x = \pm 0.01$. This restricted variation in composition was an attempt to limit inter layer diffusion; however, it also limited the variance in T_C which was in the range from -10 to 80 ^oC for the 8 materials investigated. When combined and co-sintered into an MLCC, the capacitance response was a broad peak with a maximum permittivity at ~25 ^oC and a TCC of -50% for the X7 temperature range. Although the TCC response improved compared to any of the individual materials, the lack of materials with high permittivity at the extremes of the temperature range (-55 and 125 ^oC, respectively) only improved stabilisation of the permittivity near 25 ^oC, rather than providing a significant improvement to the regions of relatively low permittivity. Although this work showed that a composite stack can be used to 'tune' the capacitance response, it also highlighted that materials selection is critical for optimisation.

One possible solution to impede diffusion is by the use of 'floating' electrodes between the materials to act as a physical barrier without being directly connected to the termination. Previously we have demonstrated the fabrication of a simple bilayer ceramic with an internal Au electrode to impede diffusion between sintered ceramics of undoped $BaTiO_3$ (BT) and $Ba_{0.975}Na_{0.025}Ti_{0.975}Nb_{0.025}O_3$ (2.5NNBT) [30]. TCC was optimised to ±6% over a ~ 100 ^oC temperature range from ~25 to 125 °C whilst

maintaining $\varepsilon_r \sim 2000$ with low dielectric loss over the range using a ratio of 0.59:0.41. Although this demonstrated proof-of-concept for a binary layer system, the temperature range where TCC was suitably low was relatively modest and also required tight constraint on the volume fraction (thicknesses) of the two layers. For example, changing the BT:2.5NNBT ratio of the bilayer to 0.55:0.45 or 0.70:0.30 from the optimum 0.59:0.41 produced TCC values >15%.

TCC temperature ranges required for MLCCs are normally much larger, for example the X9 temperature range is 255 ^oC, from -55 to 200 ^oC. As BT forms a complete solid solution with $NaNbO_3$ (NN) selecting other NNBT compositions as one of the layers to produce a bi-layer with BT may achieve a larger temperature range with low TCC but may also sacrifice the magnitude of the permittivity. The use of internal electrodes themselves however needs to be considered with care, and can lead to local compositional changes in the ceramic. Wen et al. [31] studied the interface between the dielectric and internal electrode layers in X7R-type MLCCs. A combination of SEM, EDX, and HRTEM revealed Ni from the electrode was able to diffuse into the BT perovskite lattice up to ~8 nm (via Ti-site substitution during the sintering process) and BT was able to penetrate into the electrode up to 3 nm, giving rise to a ~ 10 nm mixed region.

Conventional laboratory experiments on electroceramics are time and labour intensive and as a consequence they usually focus on in-depth characterisation of a select few 'promising' compositions from a wider series of materials. High-throughput approaches of synthesising materials have become an important approach to rapidly assess larger compositional ranges of material systems and are seen in all aspects of material science [32]. Combinatorial approaches have used atomic deposition processes to produce thin film samples with continuous or discrete compositional variations [33, 34]. There has been work in applying high-throughput methodologies to tape cast materials, which have a length scale similar to a dielectric ceramic layer in multi-layer ceramic capacitors [35].

Here we explore the potential of using such methods on a set of dielectric materials based on a perovskite solid solution. This approach can be used to rank combinations to meet TCC requirements (in the absence of electric field effects) for an extended operating temperature window whilst maintaining suitably high permittivity. The approach is resource efficient requiring only the fabrication and characterisation of the input materials, where many 100's already exist within available literature. This data can be used to generate the ε-T and TCC-T profiles for any combination of the available materials and to provide combinations that are suitable candidates for the various classifications of MLCCs. To illustrate this methodology, we have selected nine materials from the NNBT solid solution series as they exhibit a range of low electric field ε-T profiles normally explored for utilisation as dielectric materials in MLCCs.

Simulation methodology

To identify the best combination of materials and layer ratios to produce a TCC compliant MLCC, we systematically explore the range of thickness combinations for all possible material combinations. The number of combinations for a given number of input materials (without repetition) is given by

$$C(n,k) = \frac{n!}{k!\,(n-k)!}$$

Equation 2

where n represents the number of input materials and k is the number of materials in the system. In this article, we shall use 9 input materials, n = 9, and choose three to make up a tri-layer system, k=3. This generates a total 84 unique ternary combinations.

To calculate the permittivity of a layered system, each layer (material) is assumed to be an individual capacitor connected electrically in series with the others, see Figure S1(a). Equation 3 describes the resulting series capacitance C_S as a function of temperature T for our ternary system. The system depends on the individual capacitance, C(T), from each layer and can be re-written as a combination of the permittivity of free space ε_0, the relative permittivity $\varepsilon_r(T)$ and the geometric dimensions of area (A) and thickness (d) of the individual layers.

$$C_S(T) = \left[\frac{1}{C_1(T)} + \frac{1}{C_2(T)} + \frac{1}{C_3(T)}\right]^{-1} = \left[\frac{d_1}{\varepsilon_0 \varepsilon_{r_1}(T) A_1} + \frac{d_2}{\varepsilon_0 \varepsilon_{r_2}(T) A_2} + \frac{d_3}{\varepsilon_0 \varepsilon_{r_3}(T) A_3}\right]^{-1}$$

Equation 3

Equation 3 can be simplified to a dimensionless equation, as shown in equation 4, where the total series permittivity is dependent on the relative thickness fractions, d_f of the three individual dielectric layers (materials) and their individual ε values.

$$\varepsilon_S(T) = \left[\frac{d_{f,1}}{\varepsilon_1(T)} + \frac{d_{f,2}}{\varepsilon_2(T)} + \frac{d_{f,3}}{\varepsilon_3(T)}\right]^{-1} \quad \text{where } d_{f,1} + d_{f,2} + d_{f,3} = 1$$

Equation 4

To expediate the process of optimisation these equations are employed as a computational algorithm using MATLAB. We first input, from data files, the experimentally measured ε-T profiles for each material. We pre-process each input data set through spline fitting in 1°C steps across the desired temperature range. This is to ensure any noise in the experimental data does not significantly influence the optimisation process. The user then selects the required designed capacitor performance criteria, based on the codes in Table 1.
For every one of the 84 combinations, the relative thickness fraction, d_f, of each material will range between 0 and 1. We start the exploration for the optimised structure as a tri-layer system, but this can result in specific cases for the extreme values of d_f. If $d_f = 0$ is found for a specific layer, this material will then not be physically represented. This reduces the system from a ternary into a binary system of the other two materials. Unary systems can also be generated, where one material has $d_f = 1$ and the other two have $d_f = 0$. In consideration of practical applications employing tapecasting, the minimum thickness of any one layer is set at 10% of the total thickness. This corresponds to $d_f = 0.1$ on the basis that $d_f = 1.0$

(total available thickness) is of the magnitude of ~ 10 microns therefore restricting the thinnest layer to be ~ 1 micron. Beyond this limit we used increments of $d_f = 0.01$. The ternary map in Figure S1(b) illustrates the 2802 unique thicknesses explored for an individual ternary combination. For each thickness value, a permittivity profile is calculated for the different material combinations within the ternary system using equation (4). For our example of X9 classification we generated 256 permittivity values based on the temperature range of -55 to 200 °C with 1 °C increments. This generated 717,312 permittivity data points (2802 x 256) and 2802 ε-T profiles for each ternary combination.

Each of the 2802 ε-T profiles within a ternary combination is then converted into a corresponding TCC-T profile using equation (1) and the TCC-T profile performance is simplified to the maximum absolute deviation, i.e. $TCC_{abs} = \max|TCC|$. An example of a ternary TCC contour map of the 2802 TCC_{abs} values is given in Figure S1(c). This process is repeated for all 84 ternary combinations. The MATLAB algorithm then identifies the lowest (optimised) TCC which we define as TCC_{min}, for each ternary combination and ranks these from lowest (84^{th}) to highest (1^{st}) in order of decreasing TCC_{min}. It is noteworthy that during this optimisation process many of the 84 ternary combinations reduce to binary systems. This allows us to identify the 84 TCC_{min} values (one from each of the 84 ternary combinations) and to create a TCC_{min} ranking list. Thus from 9 input materials to 84 ranked optimised TCC_{min}, we generate a total of ~60 M permittivity data points (714,510 x 84). This process (excluding the time to generate the input ε-T profiles for the 9 individual materials) takes under 10 seconds on a standard desktop machine.

Optimisation over a solid solution

We first choose our input materials, here nine input ε-T profiles were selected from a single solid solution. The ceramics were prepared via the conventional solid-state route; more details are given in [30]. The ε-T profiles were obtained using an LCR meter (Agilent E4980 Precision LCR Meter, Agilent Technologies) for a fixed frequency of 100 kHz with an applied ac voltage of 100 mV and corrected for sample geometry. A selection of the ε-T profiles from the series is shown in Figure 1 and pertinent details for the full input set are summarised in Table 2. The materials were selected on the basis of their permittivity maximum, ε_{max}, being within or close to the extreme limits of the X9 temperature window. For simplicity, the materials were divided into classifications of low (L, ε_{max} between -55 to 43 °C), medium (M, ε_{max} between 76 to 122 °C) or high (H, ε_{max} at 200 °C).

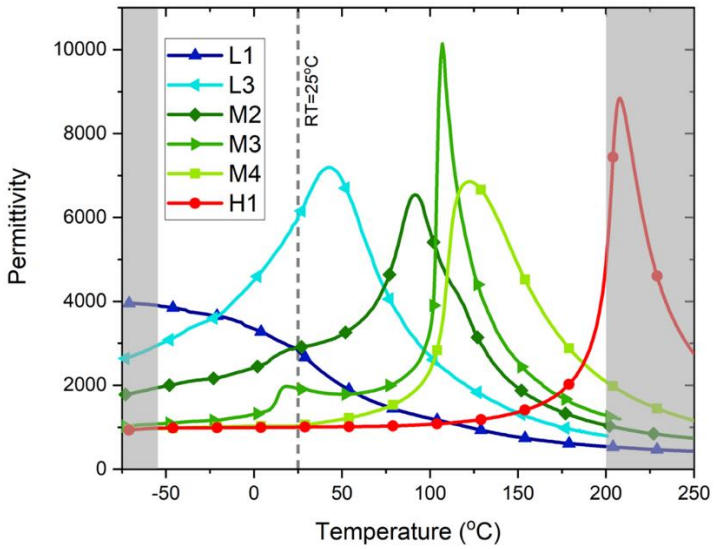

Figure 1 A selection of experimentally measured permittivity profiles included in the materials database. Labelled L, M or H depending on where ε_{max} occurs in the X9 temperature range (-55 to 200 °C). The white background indicates the X9R temperature window.

The room temperature permittivity, maximum permittivity and the temperature at which the maximum occurs (ε_{RT}, ε_{max} and T_{max}, respectively) along with the upper and lower values of TCC and TCC_{abs} are shown in Table 2. No single material and therefore unary system meets the X9 classification for any capacitor type listed in Table 1. The largest TCC_{abs} values for the L- and H-type materials occur at the highest temperature, whereas for M-type materials, the largest TCC_{abs} values occur at lower temperatures. This can be attributed to the relative difference in ε_{RT} compared to ε_{max} at $T_{max.}$ as summarised below.

- **L-type** materials possess high ε_{RT} because ε_{max} and therefore T_{max} is in close proximity to RT. TCC therefore drops substantially at high temperature resulting in large values of TCC_{abs} at 200 °C.
- **M-type** materials have lower ε_{RT} but higher ε_{max} that are located within the X9 widow. These possess high TCC values with TCC_{abs} occurring within the middle of the X9 temperature range.
- **H-type** materials have high ε_{max} leading to poor TCC at high temperatures as the permittivity is always rising from ε_{RT}. TCC_{abs} therefore occurs at 200 °C.

		Ref	Maximum			Minimum			
	Material	ε_{RT}	ε_{max}	T_{max} (°C)	TCC_{upper} (%)	ε_{min}	T_{min} (°C)	TCC_{lower} (%)	TCC_{abs} (%)
	L1	2828	3905	-55	38	541	200	**-81**	81
	L2	5520	5770	3	5	808	200	**-85**	85
	L3	6710	6725	27	0	726	200	**-89**	89
	L4	6026	7192	43	19	799	200	**-87**	87
	M1	3036	5603	76	**85**	823	200	-73	85
	M2	2903	6540	92	**125**	1048	200	-64	125
	M3	1920	10140	107	**428**	1079	-55	-44	428
	M4	1038	6855	122	**560**	966	-55	-7	560
	H1	1002	4901	200	**389**	979	-55	-2	389

Table 2 Classification and summary of the permittivity and temperature stability characteristics of the 9 materials used in the combinatorial simulations. TCC values are determined for the X9 temperature range (-55 to 200 °C).

Optimisation: simulations.

For our example, each input material is considered in 28 of the possible 84 combinations. Any two of the materials considered together are present in 7 different ternary systems. The TCC_{min} for each ternary combination is shown in figure 2 (a), and figure 2 (b) shows the ranking in terms of the materials involved.

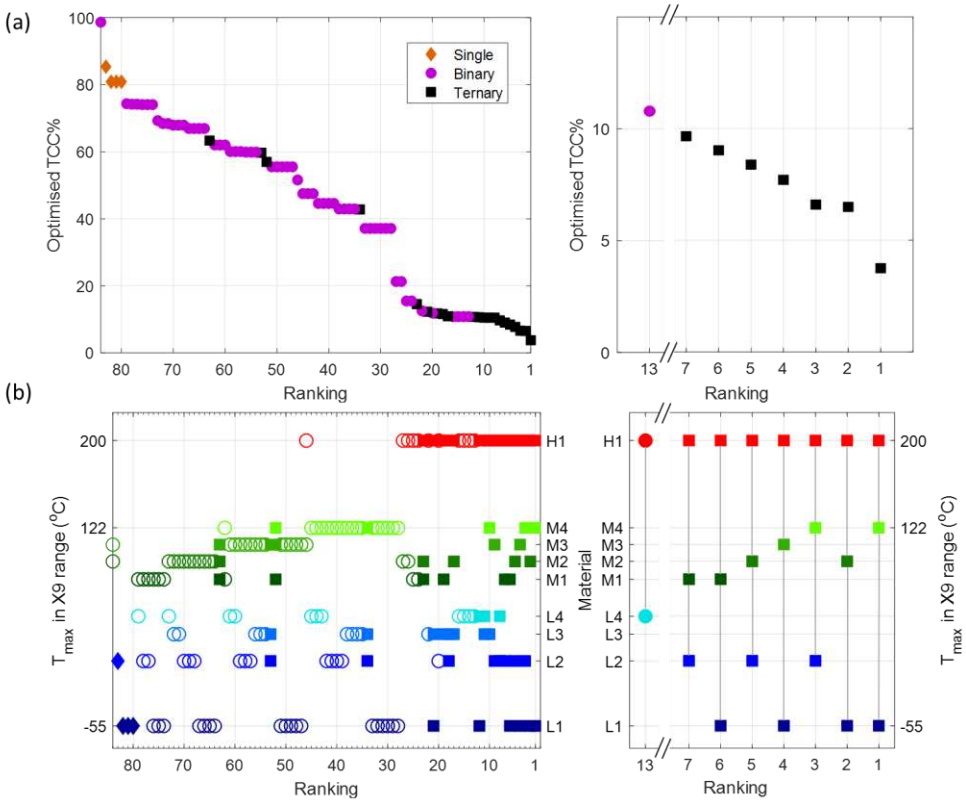

Figure 2. Output from the optimisation algorithm based on TCC_{min} for the 84 ternary material combinations. (a) TCC_{min} versus ranking for the 84 ternary combinations. (b) Variation in materials classifications for TCC_{min} optimisation. Note the best binary system (ranked 13) and seven best ternary systems (ranked 1-7). Aligned together, (a) and (b) show materials classification trends to achieve optimisation based on TCC_{min}. Note: in (b, left), filled diamonds, open circles and filled squares denote unary, binary and ternary combinations, respectively.

The right-hand side of each figure highlights optimised layer combinations for the top 7 best ranked systems and with rank 13, which represents the best bi-layer combination. The individual d_f values required to obtain TCC_{min} for each of these combinations is also given in Table 3.

	Material			d_f for each material		
Ranking	1	2	3	1	2	3
13	L4	-	H1	0.39	-	0.61
7	L2	M1	H1	0.27	0.14	0.59
6	L1	M1	H1	0.14	0.25	0.61
5	L2	M2	H1	0.28	0.16	0.56

4	L1	M3	H1	0.25	0.16	0.59
3	L2	M4	H1	0.39	0.10	0.51
2	L1	M2	H1	0.15	0.29	0.56
1	L1	M4	H1	0.31	0.19	0.50

Table 3. Selected TCC_{min} ranked ternary systems showing the materials involved and their d_f values. Rank 13 is the best bi-layer combination and ranks 7 to 1 are the top 7 tri-layer combinations.

Although these data capture TCC_{min} for each ternary system, Figure 3 compares the lowest TCC for the best bilayer and trilayer combinations for the top 20 ranked systems where TCC ≤ 15% and therefore within X9R classification. The ε-T and TCC-T profiles for the optimised bilayer (rank 13) and trilayer (rank 1) combinations are shown in Figure 4. The salient features from figures 1-4 are discussed below.

(i) Of the 84 combinations, optimisation leads to 4 single, 59 binary and 21 ternary systems, Figure 2 (a).

(ii) Between ranking 33 to 28, L1 and M4 combine 6 times within different ternary combinations where the third material is another L or M to produce a bilayer with a TCC_{min} of ~ 37%. Only with the addition of H1 to form a trilayer does the ternary combination outperform this. The optimised L1-M4-H1 trilayer outperforms all other combinations with TCC_{min} of 4%, Figure 2(a) and (b).

(iii) The best binary combination is a bilayer of L4-H1 (rank 13) with a ratio of 0.39:0.61, and TCC_{min} ~ 10.5%, Figure 2 (a), (b) and Table 3.

(iv) The 7 highest ranking combinations based on TCC_{min} are trilayers that each contain a L, M and H material, see black squares in Figure 2(a) and 2 (b) and can achieve X9P classification. The optimised trilayer (rank 1) achieves a 2.8 times improvement of TCC_{min} compared to the optimised bilayer (rank 13), Figure 3. Combinations that contain two L or two M materials rarely optimise as ternary systems with only one of them featuring in a final optimised bilayer. The top 27 ranked combinations all contain H1 and perform noticeably better in TCC. This is due to the addition of a high temperature ε_{max} material that restricts the severe drop-off in TCC for all L and M1-3 materials at the upper temperature of the X9 range, Figure 1 and Table 2.

(v) The significance of $T_{max.}$ is apparent from figure 2 (b) where the highest ranked combinations are those with the largest spread in T_{max}. This is shown where L1 outperforms L2 when combined with the same M and H materials, ranked 1 and 3, respectively. The position of T_{max} is not the only significant factor, the shape of the ε–T profile is also important. The combination of L1-M2-H1 (rank 2) outperforms L1-M3-H1 (rank 4) in TCC_{min} by 3%, figure 2 (b), despite M2 having a lower T_{max} and ε_{max} than M3, Figure 1 and Table 2. M2 has a broader and lower permittivity profile than M3, allowing better TCC stability in the middle of the X9 temperature window, Figure 1. Materials L3 and L4 do not appear in any of the L-M-H combinations that meet X9P.

(vi) Bilayers of H1 combined with L1-4 can achieve TCC ~ 11-13% (red symbols in Fig 3(a)), Figure 3.

(vii) Various trilayers based on L-L-H and L-M-H combinations have similar TCC values (blue symbols in Fig 3(a) for rankings 20 to 8) to those of L-H bilayers highlighted in (v) by the red symbols in Fig 3(a). Adding a third layer (either L or M) or replacing L4 with a combination of L and M materials for these rankings has very little (if any) improvement on TCC_{min} compared to the best bilayer combination of L4-H1 (rank 13).

(viii) There is a distinct improvement in TCC for trilayers over bilayers for rankings 7 to 1, Figure 3, due to clear divergence in T_{max} for the L and M materials and the balanced combination of L-M-H materials.

To illustrate some of these features we discuss the ε-T and TCC-T profiles for the TCC_{min} optimised bilayer (rank 13) and trilayer (rank 1).

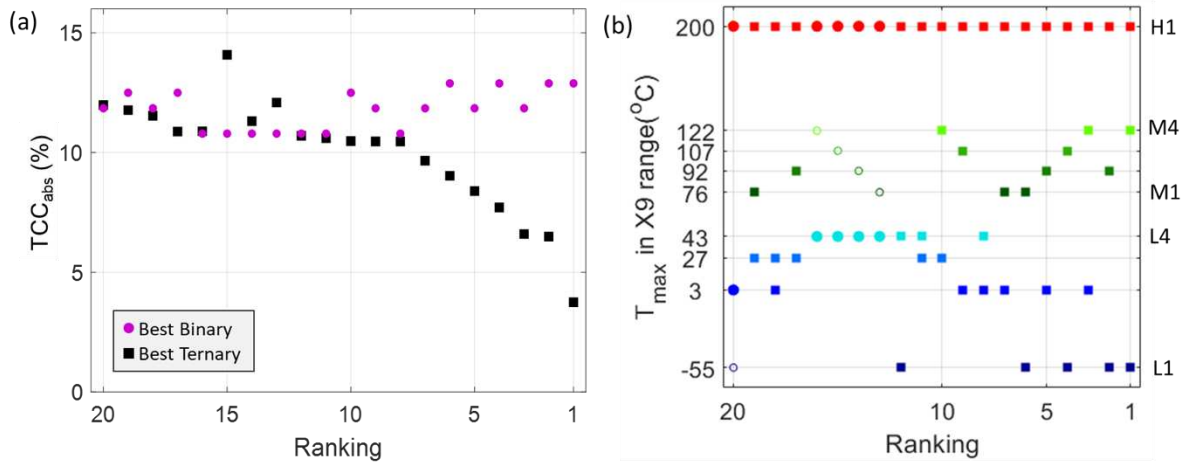

Figure 3 (a) The lowest TCC for the best bilayers and trilayers from the top 20 ranked combinations. (b) The Materials involved in the top twenty ranked combinations. In (b), open symbols in ranks 15-13 indicate the third starting material which optimised out of the system with $d_f = 0$.

The optimised bilayer has its TCC_{lower} at -55^{o}C, and TCC_{upper} at 200^{o}C. As the permittivity of the two materials combine in a reciprocal manner, equation 4, the permittivity of the bilayer tends towards the lower permittivity material (for similar values of d_f). L4 allows for suppression of the large TCC_{upper} of H1 at 200^{o}C, and H1 suppresses TCC_{lower} of L4, fig 4 (a), black line. At the optimised d_f ratio, the two turning points of the TCC profile are reasonably well balanced and allow TCC_{lower} and TCC_{upper} to be within X9R specification, Figure 4 (b), black line. This balancing, however, leads to this binary system being sensitive to changes in d_f, i.e X9R is met only for x = 0.38 – 0.44 with optimisation at x = 0.39.

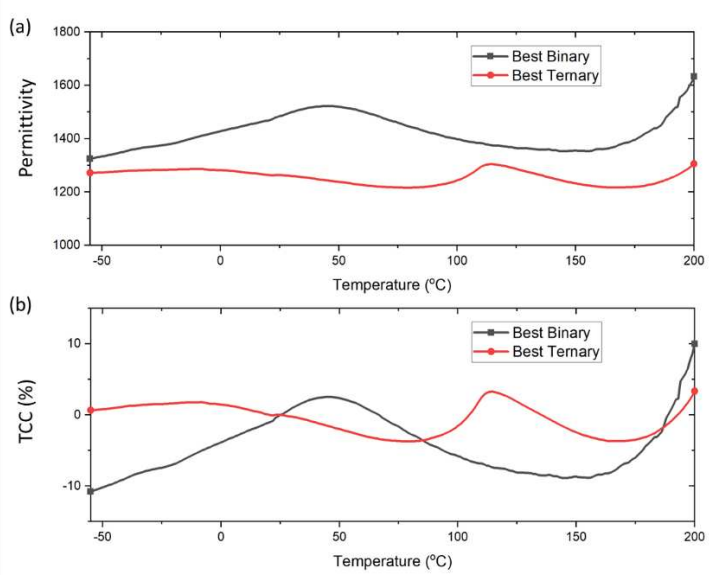

Figure 4. Comparison of the combinations that optimise as the best binary (L4-H1) and the best ternary (L1-M4-H1). (a) The ε-T profiles at the optimised d_f values of 0.39:0.61 and 0.31:0.19:0.50, respectively, and (b) the corresponding TCC profiles.

The optimised trilayer (rank 1) can achieve X9P classification due to the flatter ε-T profile, figure 4 (a) red line, due to the distribution of the three T_{max} values (i.e. -55, 122 and 200 °C, respectively) across the X9 window. The ε-peak of one material is suppressed by the other two leading to four turning points in the TCC-T profile, figure 4 (b) red line, compared to the two turning points in the binary, figure 4 (b) black line. The increased number of turning points allow TCC to be 'rotated' back into the X9P specification as successive turning points occur.

The importance of how the third material can influence the optimisation is illustrated in figure 5 for the TCC contour map of L1-M4-H1. Here we show the effect of (i) adding M4 into the best binary (L4-H1) and (ii) adding H1 into the L1-M4 binary. Both lead to the optimised TCC_{min} within the ternary system (rank 1) indicated by the yellow star in Figure 5(a). This optimisation can be viewed as an animated gif in Figure S1(d)

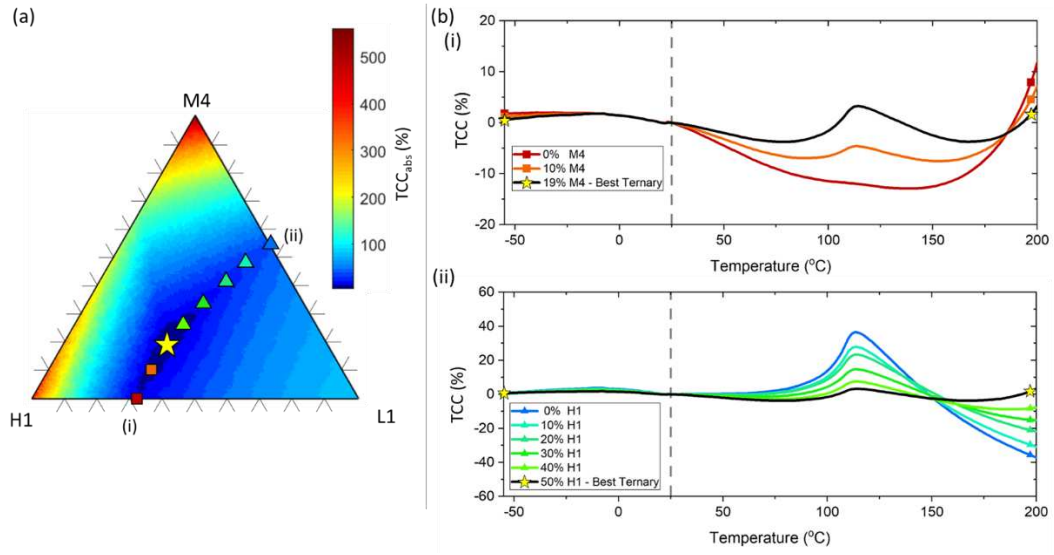

Figure 5. (a) The TCC contour map of the ternary system L1-M4-H1. The coloured symbols follow a lowering of TCC to obtain TCC_{min} (yellow star symbol) within the ternary system starting from the lowest TCC values

associated with the H1-L1, point (i), and M4-H1, point (ii) binary systems. (b) (i) and (ii) are the TCC-T profiles that illustrate the influence of a third material (M4 and H1, respectively) on the binary systems of H1-L1 and L1-M4 to achieve TCC_{min}.

Starting on the L1-H1 binary system with the optimised d_f ratio of 0.39:0.61, point (i) in figure 5a, there is a drop in TCC between 100-150 ^oC, whereas it rises steeply from ~ 175 to 200 ^oC, figure 5 b (i). As the M4 profile possesses a ε peak at 122 ^oC with decreasing ε at 200^oC, it works well as an addition in this region of the X9 window. Increasing the d_f of M4 from 0.00 to 0.19, increases the overall ε at 100-150 ^oC whilst decreasing it at higher temperatures. This flattens the overall TCC profile and meets X9P specification, figure 5b (i). The optimised d_f ratio on the L1-M4 binary system, point (ii) in Figure 5 (a), has a large peak in TCC at ~ 122 ^oC and a large and negative TCC at 200 ^oC. These features are associated with the ε peak of M4 and the absence of the high ε of H1 at higher temperatures. Increasing the d_f of H1 from 0.00 to 0.50 suppresses the ε peak associated with M4 and increases the overall permittivity at higher temperatures thus suppressing both the TCC peak at ~122 ^oC and the large negative TCC at 200 ^oC to achieve X9P classification, figure 5b (ii).

Optimisation: experimental verification

Identification of how to achieve TCC_{min} optimisation based on these material sets allows key ceramics to be combined in different thicknesses to validate the simulations and to replicate the TCC contour map and profiles shown in Figure 5. Ceramics of L1, M4 and H1 were prepared by the solid state method described previously [30] and their major faces coated with Au paste electrodes. The ceramics were stacked electrically in series to replicate bilayers or trilayers with the relative thicknesses of the ceramics representing their d_f. With initial thicknesses of 0.86, 0.83 and 4.51 mm for L1, M4 and H1 ceramics, respectively this allowed experimental ε-T profiles to be measured for L1-M4, L1-H1 and M4-H1 bilayers at points 1, 2 and 3 and for an L1-M4-H1 trilayer at point 4 in the ternary system as shown in Figure 6.

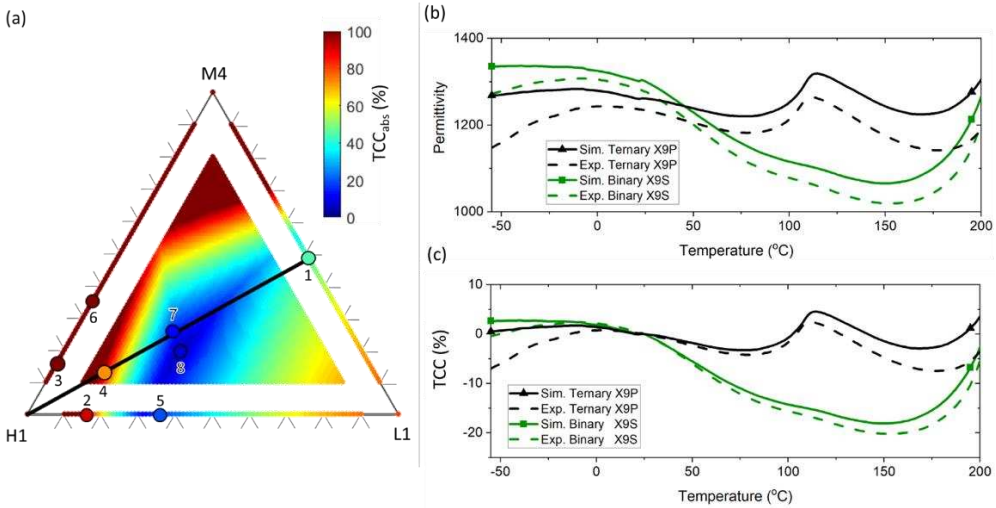

Figure 6. (a) The TCC contour map for the ternary system L1-M4-H1 with selected points (1-8) to indicate bilayer or trilayer combinations of ceramics used for experimental verification. (b) and (c) show the permittivity and TCC comparisons for simulated and experimentally measured samples of an X9S bilayer (point 5) and an X9P trilayer (point 8). The Internal triangle in (a) is the window where $d_f \geq 0.1$.

Selective thinning of the ceramics created various d_f values, allowing other bilayers (points 5 and 6) and trilayers (7 and 8) to be investigated with samples 4, 7 and 1

being on a tie line between bilayer 1 (L1-M4) and H1 and sample 8 close to the 0.31:0.19:0.50 ratio required to obtain TCC_{min} based on the simulations. The list of pellet thicknesses and d_f values for the various bi- and tri-layers along with TCC (simulation) compared to TCC (experimental) are given in Table 4. The solid lines in figure 7(b) and (c) are the simulated profiles based on those d_f values, meeting the classifications of X9P (point 8) and X9S (point 5). The dashed lines are the experimental verification based on the results from the ceramics. The ε-T and TCC-T profiles obtained from the experimental results closely follow the simulated profiles but possess lower than predicted ε. The measured permittivity is ~2% lower than that simulated at room temperature, increasing to ~9% at both -55 and 200 ºC for the trilayer. The bilayer behaves similarly, with the measured permittivity being ~ 4% lower at room temperature and rising to ~7% at the X9 temperature limits. This permittivity decrease affects TCC of the measured samples but not enough to cause them to fail the predicted specification. The lower ε values are attributed to contact interfaces between the ceramics in the bi- and tri-layer samples.

No.	Pellet Thickness (mm)			Total Thickness (mm)	df of material			Simulation	Experimental
	L1	M4	H1		L1	M4	H1	TCC_{abs} (%)	TCC_{abs} (%)
1	0.86	0.83	-	1.69	0.51	0.49	-	44.5	44.9
2	0.86	-	4.51	5.37	0.16	-	0.84	91.4	91.6
3	-	0.83	4.51	5.34	-	0.16	0.84	302.2	264.1
4	0.84	0.83	4.51	6.18	0.14	0.13	0.73	95.0	72.4
5	0.84	-	1.52	2.36	0.36	-	0.64	18.1	20.2
6	-	0.83	1.52	2.35	-	0.35	0.65	227.3	164.1
7	0.84	0.83	1.52	3.19	0.26	0.26	0.48	15.9	11.4
8	0.84	0.55	1.34	2.73	0.31	0.20	0.49	4.6	7.5

Table 4. Thickness and d_f values of ceramics along with TTC_{abs} values for simulations and experiments based on eight points (1-8) illustrated in Figure 6 (a).

Further Optimisations: (i) TCC classification and (ii) room temperature permittivity.

(i) Although optimisation for X9P provides a high specification capacitor based on trilayers it is not the only commercially viable option. With the use of this code, optimisation for TCC associated with other classifications is possible, as shown in figure 7. Here the smallest (black) region highlights the tightest classification of X9P and this can only be obtained from ternary combinations. The optimised combination of 0.31:0.19:0.50 for L1-M4-H1 lies close to the centre of the black area and indicates there is a level of variation in d_f values within the ternary diagram where X9P can be achieved. This is potentially useful for any small variations in d_f values during processing of MLCCs. Relaxing the TCC classification from P=$\pm$10% to R=$\pm$15% generates additional sets of combinations, shown in the yellow region. Lowering the tolerance of TCC for the other classifications shown in table 1 down to X9V (+22 to -82%) yields viable combinations as shown by the other coloured regions in figure 7. TCC classification of P, R and S are symmetrical causing the optimised coloured region to maintain their shape; however, T, U and V classifications are asymmetrical and this permits greater negative deviation in TCC_{lower} than positive TCC_{upper} and results in these regions expanding towards

combinations with increased d_f of L1. For these latter classifications it is clear that bilayers have a wide d_f tolerance window and offer a simpler practical solution as opposed to the use of trilayers.

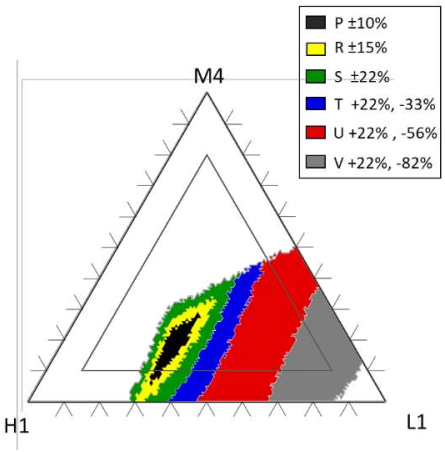

Figure 7. Simulated regions of the L1-M4-H1 ternary system that achieves different TCC classifications.

(ii) The main optimisation parameter in this script has been low electric field TCC; however, other parameters are important for MLCC manufactures, such as the room temperature permittivity, ε_{RT}. This is an output that our code can also generate in the TCC_{min} ranking process as shown in figure 8. The general trend followed is that combinations that possess high ε_{RT} generally lead to a poor TCC_{min}.

As the permittivity tends to the lowest value (for a series type combination), materials with low $\varepsilon_{RT,}$ will reduce the overall permittivity of the device. In our example, the use of H1 provides the ability to increase the TCC operational temperature window (high T_{max} of 200 °C) but has the lowest ε_{RT} (1002) of the nine available materials, Table 1. 27 of the 28 combinations that include H1 result in TCC_{min} being < 22 %, Figure 2; however, there are significant variations in ε_{RT}, see inset in Figure 8. This may influence the final choice of material combinations for MLCC production.

Optimisation of TCC_{min} is favourable with T_{max} of the materials spread across the temperature range using a combination of L-M-H materials; however, ε_{RT} is enhanced by those with T_{max} near RT. From the 7 combinations in our example that optimise for X9P, the top ranked combination of L1-M4-H1 has both the lowest TCC_{min} and ε_{RT}, Figure 8. The 3rd ranked combination however of L2-M4-H1 offers an alternative option that comfortably achieves X9P specification (TCC_{min} ~ 6.5 %) but with an increase in ε_{RT} of ~1500. The higher ε_{RT} is attributed to the T_{max} values of L2 (3 °C) and M2 (92 °C) being closer to RT compared with L1 (-55 °C) and M4 (122 °C) in the top ranked combination, Figure 1 and Table 1.
As a consequence, the 3rd ranked combination of L2-M4-H1 based on TCC_{min} may be a better overall choice for MLCC production given the ~ 20% enhancement in ε_{RT}.

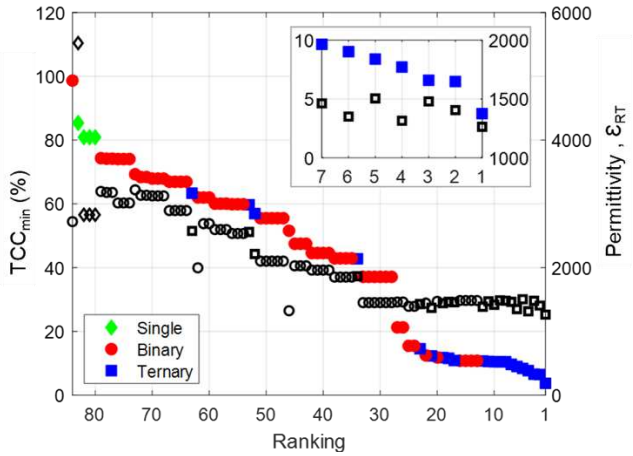

Figure 8 Ranked optimised TCC_{min} for the 84 combinations (coloured symbols), with an overlay of corresponding room temperature permittivity (open black squares). Inset shows TCC_{min} and room temperature permittivity for the top seven ranked ternary systems on an expanded scale.

Limitations and future directions

Although our approach does present a resource efficient starting point based on TCC it has several limitations and challenges. We outline three below.

(i) Availability of VCC data. Here we have focussed on the low electric field dielectric properties of bulk ceramics to assist with materials selection and have based our criterion on optimising TCC first, and then ε_{RT}. In practice, the design of MLCCs requires dielectric layers of ~ 1- 10 microns. At such thicknesses there are several critical parameters that influence TCC and ε_{RT} based on size and scaling effects [16,18] that we have not considered, e.g. grain size, microstructure, the number of grain boundaries and voltage effects. Consideration of VCC is particularly important as it is known to influence TCC in thin dielectric layers of $BaTiO_3$-based formulations. To experimentally assess VCC requires ε-T measurements to be performed as a function of dielectric thickness (typically below ~ 10 microns) and under high electric fields (typically ~ 10's kV/cm). As a consequence, VCC data is not easily available for bulk ceramics and is rarely reported for proto-type MLCCs in the literature. This limits our present approach to consider TCC in the absence of electric field effects.

(ii) Interdiffusion, pO_2 stability and electrode effects. Our approach is based on dense ceramics being physically separated by Au electrodes prior to electrical characterisation. This avoids the interdiffusion effects that occur during processing of MLCCs based on layers with different composition and which lead to significant deviations between modelled and experimental TCC profiles [28, 29]. Such effects could be limited by selecting materials that have similar compositions or by the use of floating electrodes within MLCCs to restrict interdiffusion. Furthermore, the majority of MLCCs use Ni as internal electrodes and are processed under reducing conditions at high temperatures. All potential materials identified would have to be tested for their ability to withstand these processing conditions and be compatible with Ni electrodes prior to MLCC development.

(iii) Resistivity. The calculations used in our approach are based only on permittivity and do not include the resistivity of the materials. Resistivity is an important parameter for bi- or tri-layered MLCCs as the potential difference across each material will be different. This will influence the electric field across each layer and therefore TCC.

Future work is currently underway to implement a description of the voltage effect into the prediction tool. A combination of VCC measurements with fitting from Johnson's approximation [27, 36] should allow some prediction on the influence of VCC on TCC. Further optimisation of voltage dependency to include features associated with grain size may be achieved by modifying the Johnson parameter [27]. Interdiffusion and electrode effects of the layers are also being considered through linking to atomic scale simulations. This will permit incorporation of intermediate layers and contact impedances into the model.

In conclusion, we have presented and experimentally verified an efficient combinatorial method for the optimisation of materials for multi-layer ceramic capacitors (MLCCs) based on bilayer or trilayer combinations of materials. Experimental ε-T data from nine materials were used to generate ~ 60 M permittivity data points over the X9 classification temperature range for 84 unique ternary systems based on varying individual layer thicknesses. An algorithm was used to rank performance based on the low electric field TCC_{min} for each system; however, additional factors such as ε_{RT} and the justification for tri- as opposed to bi-layers were also considered in selecting the most appropriate combination of materials.

Our example demonstrated how to identify a subset of 7-8 ternary and a 'best binary' combination of materials with X9R classification. Although the example was based on experimental input from nine materials within a single solid solution phase there is (in principle) no limit to the number of input materials. A much wider range of materials can be explored; however, chemical compatibility, interdiffusion, microstructural control and the sintering characteristics of the individual materials remain practical issues that require investigation.

Finally, our method to assist with materials selection is based on TCC and ε_{RT} obtained from the low electric field dielectric properties of bulk ceramics. Future developments require consideration of the VCC and resistivity of the materials. These parameters are especially critical in the development of high voltage and/or temperature X8R (and beyond) MLCCs. The approach is therefore a resource efficient *starting point* for the development cycle of engineered dielectrics for MLCC applications. It should be viewed as a prerequisite to the necessity of focussing on microstructural control, chemical and electrode compatibility and the development of critical MLCC characteristics (in addition to TCC and ε_{RT}) such as VCC, Life-time and EBS.

Acknowledgements.
We thank the Engineering and Physical Science Research Council (EPSRC) for a studentship (GK) and for financial support: EP/L017563/1; Substitution and Sustainability in Functional Materials and Device; DCS and JSD, and EP/P019919/1; Charging Ahead with Multi-Layer Ceramic Capacitor Materials; JSD.

References.

[1] H. Kishi, Y. Mizuno, and H. Chazono, "Base-metal electrode-multilayer ceramic capacitors: Past, present and future perspectives," *Japanese Journal of Applied Physics Part 1-Regular Papers Short Notes & Review Papers,* Review vol. 42, no. 1, pp. 1-15, Jan 2003, doi: 10.1143/jjap.42.1.

[2] "Global Multilayer Ceramic Capacitor (MLCC) Market, by Type (Class I (NP0/C0G, U2J, others), Class II (X7R, X5R, Y5V, Z5U), by Application (Consumer Electronics, Automotive, Manufacturing, Telecommunication, Transportation, Healthcare). Forecast till 2024", ID: MRFR/SEM/6269-HCR. Market research future, Available from https://www.marketresearchfuture.com/reports/multilayer-ceramic-capacitor-market-7738 (last accessed Auguest 2020)

[3] D. Wolfe, "The global shortage of capacitors impacts all consumer electronics ",Quartz Media, March 2019.

[4] K. J. Park, C. H. Kim, Y. J. Yoon, S. M. Song, Y. T. Kim, and K. H. Hur, "Doping behaviors of dysprosium, yttrium and holmium in $BaTiO_3$ ceramics," *Journal of the European Ceramic Society,* Article vol. 29, no. 9, pp. 1735-1741, Jun 2009, doi: 10.1016/j.jeurceramsoc.2008.10.021.

[5] M. Y. Liu *et al.*, "Temperature stability of dielectric properties for $xBiAlO_3$-(1-x)$BaTiO_3$ ceramics," *Journal of the European Ceramic Society,* Article vol. 35, no. 8, pp. 2303-2311, Aug 2015, doi: 10.1016/j.jeurceramsoc.2015.02.015.

[6] L. Gong, X. H. Wang, S. P. Zhang, H. Wen, and L. T. Li, "Grain size effect on electrical and reliability characteristics of modified fine-grained $BaTiO_3$ ceramics for MLCCs," *Journal of the European Ceramic Society,* Article vol. 34, no. 7, pp. 1733-1739, Jul 2014, doi: 10.1016/j.jeurceramsoc.2013.12.028.

[7] T. R. Armstrong and R. C. Buchanan, "Influence of core shell grains on the internal-stress state and permittivity response of zirconia-modified barium-titanate," *Journal of the American Ceramic Society,* Article vol. 73, no. 5, pp. 1268-1273, May 1990, doi: 10.1111/j.1151-2916.1990.tb05190.x.

[8] F. D. Morrison, D. C. Sinclair, and A. R. West, "Electrical and structural characteristics of lanthanum-doped barium titanate ceramics," *Journal of Applied Physics,* Article vol. 86, no. 11, pp. 6355-6366, Dec 1999, doi: 10.1063/1.371698.

[9] K. Yasukawa, M. Nishimura, Y. Nishihata, and J. Mizuki, "Core-shell structure analysis of $BaTiO_3$ ceramics by synchrotron X-ray diffraction," *Journal of the American Ceramic Society,* Article vol. 90, no. 4, pp. 1107-1111, Apr 2007, doi: 10.1111/j.1551-2916.2007.01537.x.

[10] M. Y. Liu *et al.*, "Preparation and dielectric properties of X9R core-shell $BaTiO_3$ ceramics coated by $BiAlO_3$-$BaTiO_3$," *Ceramics International,* Article vol. 42, no. 1, pp. 379-387, Jan 2016, doi: 10.1016/j.ceramint.2015.08.120.

[11] C. A. Randall, S. F. Wang, D. Laubscher, J. P. Dougherty, and W. Huebner, "Structure property relationships in core-shell $BaTiO_3$-LiF ceramics," *Journal of Materials Research,* Article vol. 8, no. 4, pp. 871-879, Apr 1993, doi: 10.1557/jmr.1993.0871.

[12] Z. H. Yao, H. X. Liu, Y. Liu, Z. H. Wu, Z. Y. Shen, and M. H. Cao, "Structure and dielectric behavior of Nd-doped $BaTiO_3$ perovskites," *Materials Chemistry and Physics,* Article vol. 109, no. 2-3, pp. 475-481, Jun 2008, doi: 10.1016/j.matchemphys.2007.12.019.

[13] H. I. Hsiang, F. S. Yen, and C. Y. Huang, "Effects of porosity on dielectric-properties of $BaTiO_3$ ceramics," *Japanese Journal of Applied Physics Part 1-Regular Papers Short Notes & Review Papers,* Article vol. 34, no. 4A, pp. 1922-1925, Apr 1995, doi: 10.1143/jjap.34.1922.

[14] G. Arlt, D. Hennings, and G. Dewith, "Dielectric-properties of fine-grained barium-titanate ceramics," *Journal of Applied Physics,* Article vol. 58, no. 4, pp. 1619-1625, 1985, doi: 10.1063/1.336051.

[15] V. Buscaglia and C. A. Randall, “Size and scaling effects in barium titanate. An overview,” *Journal of the European Ceramic Society*, Article vol, 40, pp. 3744-3758, 2020, doi.org/10.1016/j.jeurceramsoc.2020.01.021.

[16] K. Hong, T. H. Lee, J. M. Suh, J. S. Park, H. S. Kwon, J. Choi and H. W. Jang, “Direct observation of surface potential distribution in insulation resistance degraded acceptor-doped $BaTiO_3$ multilayered ceramic capacitors”. *Electronic Materials Letters*, Article vol. 14, no. 5, pp 629-635, 2018, https://doi.org/10.1007/s13391-018-0066-6.

[17] K. Hong, T. H. Lee, J. M. Suh, S. H. Yoon and H. W. Jang, “Perspectives and challenges in multilayer ceramic capacitors for next generation electronics”. *Journal of Materials Chemistry C*, Article vol 7, no 32, pp 9782-9802, 2019, doi: 10.1039/c9tc02921d.

[18] M. T. Buscaglia, M. Viviani, Z. Zhao, V. Buscaglia, and P. Nanni, "Synthesis of $BaTiO_3$ core-shell particles and fabrication of dielectric ceramics with local graded structure," *Chemistry of Materials,* Article vol. 18, no. 17, pp. 4002-4010, Aug 2006, doi: 10.1021/cm060403j.

[19] C. H. Kim, K. J. Park, Y. J. Yoon, D. S. Sinn, Y. T. Kim, and K. H. Hur, "Effects of milling condition on the formation of core-shell structure in $BaTiO_3$ grains," *Journal of the European Ceramic Society,* Article vol. 28, no. 13, pp. 2589-2596, Sep 2008, doi: 10.1016/j.jeurceramsoc.2008.03.030.

[20] M. T. Benlahrache, N. Benhamla, and S. Achour, "Dielectric properties of $BaTiO_3$-$NaNbO_3$ composites," *Journal of the European Ceramic Society,* Article; Proceedings Paper vol. 24, no. 6, pp. 1493-1496, 2004, doi: 10.1016/s0955-2219(03)00577-6.

[21] Y. Sun, H. X. Liu, H. Hao, Z. Song, and S. J. Zhang, "Structure Property Relationship in $BaTiO_3$-$Na_{0.5}Bi_{0.5}TiO_3$-Nb_2O_5-NiO X8R System," *Journal of the American Ceramic Society,* Article vol. 98, no. 5, pp. 1574-1579, May 2015, doi: 10.1111/jace.13517.

[22] J. S. Dean, J. H. Harding, and D. C. Sinclair, "Simulation of Impedance Spectra for a Full Three-Dimensional Ceramic Microstructure Using a Finite Element Model," *Journal of the American Ceramic Society,* Article vol. 97, no. 3, pp. 885-891, Mar 2014, doi: 10.1111/jace.12750.

[23] J. P. Heath, J. S. Dean, J. H. Harding, and D. C. Sinclair, "Simulation of Impedance Spectra for Core-Shell Grain Structures Using FiniteElement Modeling,", *Journal of the American Ceramic Society,* Article vol. 98, no. 6, pp. 1925-1931, Jun 2015, doi: 10.1111/jace.13533.

[24] J. P. Heath, J. H. Harding, D. C. Sinclair, J. S. Dean, The Analysis of Impedance Spectra for Core–Shell Microstructures: Why a Multiformalism Approach is Essential. Advanced Function Materials, Article vol. 29, pp. 1904036- 1904036, 2019. doi: 10.1002/adfm.201904036

[25] J. S. Dean, P. Y. Foeller, I. M. Reaney, and D. C. Sinclair, "A resource efficient design strategy to optimise the temperature coefficient of capacitance of $BaTiO_3$-based ceramics using finite element modelling," *Journal of Materials Chemistry A,* Article vol. 4, no. 18, pp. 6896-6901, 2016. doi: 10.1039/c5ta09573e

[26] J. P. Heath, J. H. Harding, D. C. Sinclair, and J. S. Dean, "Electric field enhancement in ceramic capacitors due to interface amplitude roughness,", *Journal of the European Ceramic Society,* Article vol. 39, no. 4, pp. 1170-1177, Apr 2019, doi: 10.1016/j.jeurceramsoc.2018.10.033.

[27] L. Padurariu, L. Curecheriu, V. Buscaglia and L. Mitoseriu, “Field-dependent permittivity in nanostructured $BaTiO_3$ ceramics:Modeling and experimental verification,” *Physical Review B*, Article vol. 85, 224111, 2012, doi: 10.1103/PhysRevB.85.224111.

[28] T. M. Amaral, E. Antonelli, D. A. Ochoa, J. E. Garcia, and A. C. Hernandes, "Microstructural Features and Functional Properties of Bilayered $BaTiO_3$/$BaTi_{1-x}Zr_xO_3$ Ceramics," *Journal of the American Ceramic Society,* Article vol. 98, no. 4, pp. 1169-1174, Apr 2015, doi: 10.1111/jace.13417.

[29] H. C. Song, J. E. Zhou, D. Maurya, Y. K. Yan, Y. U. Wang, and S. Priya, "Compositionally Graded Multilayer Ceramic Capacitors," *Scientific Reports,* Article vol. 7, p. 12, Sep 2017, Art no. 12353, doi: 10.1038/s41598-017-12402-7.

[30] P. Y. Foeller, J. S. Dean, I. M. Reaney, and D. C. Sinclair, "Design of a bilayer ceramic capacitor with low temperature coefficient of capacitance," *Applied Physics Letters,* Article vol. 109, no. 8, p. 4, Aug 2016, Art no. 082904, doi: 10.1063/1.4961616.

[31] H. Wen, X. H. Wang, and L. T. Li, "Observation on the interdiffusion in multilayer ceramic capacitors," *Japanese Journal of Applied Physics Part 1-Regular Papers Brief Communications & Review Papers,* Article vol. 45, no. 3A, pp. 1768-1770, Mar 2006, doi: 10.1143/jjap.45.1768.

[32] R. Potyrailo, K. Rajan, K. Stoewe, I. Takeuchi, B. Chisholm, and H. Lam, "Combinatorial and High-Throughput Screening of Materials Libraries: Review of State of the Art," *Acs Combinatorial Science,* Review vol. 13, no. 6, pp. 579-633, Nov-Dec 2011, doi: 10.1021/co200007w.

[33] S. Guerin and B. E. Hayden, "ABO_3 and $A_{1-x}C_xB_{1-y}D_y(O_{1-z}E_z)_3$: review of experimental optimisation of thin film perovskites by high-throughput evaporative physical vapour deposition," *Chemical Communications,* Review vol. 55, no. 68, pp. 10047-10055, Sep 2019, doi: 10.1039/c9cc03518d.

[34] P. J. McGinn, "Thin-Film Processing Routes for Combinatorial Materials Investigations-A Review," *Acs Combinatorial Science,* Review vol. 21, no. 7, pp. 501-515, Jul 2019, doi: 10.1021/acscombsci.9b00032.

[35] R. C. Pullar, "Combinatorial Bulk Ceramic Magnetoelectric Composite Libraries of Strontium Hexaferrite and Barium Titanate," *Acs Combinatorial Science,* Article vol. 14, no. 7, pp. 425-433, Jul 2012, doi: 10.1021/co300036m.

[36] K. M. Johnson, “Variation of Dielectric Constant with Voltage in Ferroelectrics and Its Application to Parametric Devices”, *Journal of Applied Physics* Article vol. 33, 2826-2831 (1962) doi.org/10.1063/1.1702558

Supplementary Information.

Resource Efficient Exploration of Ternary Phase Space to Develop Multi-Layer Ceramic Capacitors

G. Kerridge, D. C. Sinclair and J. S. Dean
Department of Materials Science & Engineering, Sir Robert Hadfield Building, University of Sheffield, Mappin Street, UK, S1 3JD.

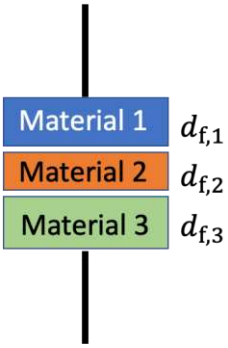

Figure S1 (a). Schematic diagram showing the trilayer arrangement of a capacitor with three different materials connected (electrically) in series.

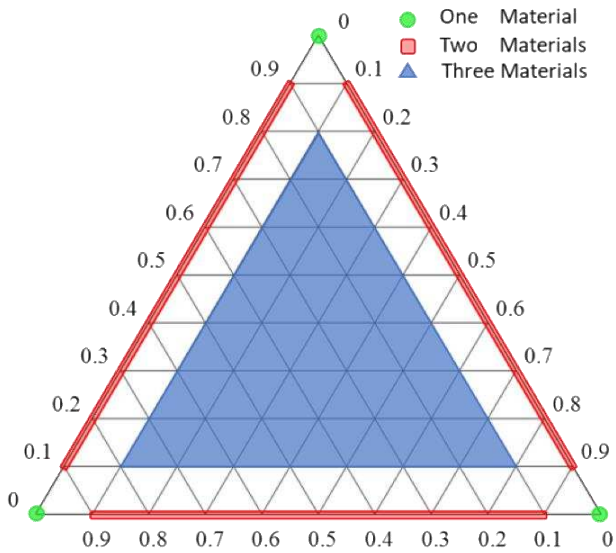

2802 = $3_{Uni} + 243_{Bin} + 2556_{Tern}$

$d_{f1} = 1, d_{f(2,3)} = 0$
$d_{f2} = 1, d_{f(1,3)} = 0$
$d_{f3} = 1, d_{f(1,2)} = 0$
1 point defining range
$N_{Uni} = 3$

$0.1 \geq d_{f(1,2)} \leq 0.9, d_{f3} = 0$
$0.1 \geq d_{f(1,3)} \leq 0.9, d_{f2} = 0$
$0.1 \geq d_{f(2,3)} \leq 0.9, d_{f1} = 0$
81 points defining ranges
$N_{Bin} = 81x3 = 243$

$0.1 \geq d_{f(1,2,3)} \leq 0.8$
71 points defining range. Upper d_f of 0.8 as combined with 2 x d_f =0.1.

$$N_{Tern} = \sum_{k=1}^{k=71} k = \frac{k^2 + k}{2} = \frac{71^2 + 71}{2} = 2556$$

Figure S1 (b). Schematic of a ternary map that illustrates how 2802 unique thicknesses are generated and explored for an individual ternary combination of three different materials. Green symbols represent the 3 unary systems, the red symbols represent the 243 data points associated with the three binary systems (81 points per system) and the shaded blue triangle represents the 2556 points within the ternary system. Total explored was 3 + 243 + 2556 = 2802.

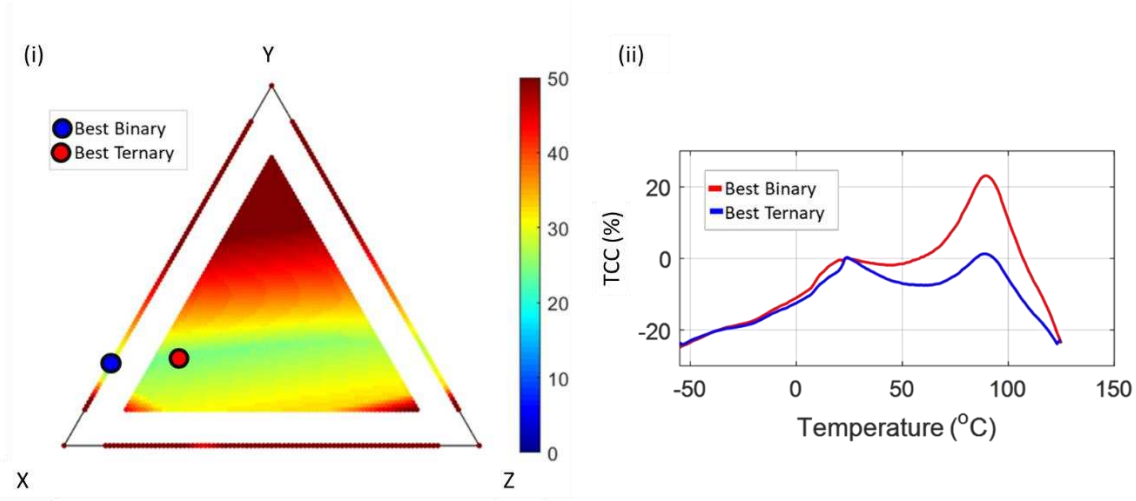

Figure S1 (c). (i) Example of a TCC contour map of a ternary system X-Y-Z. TCC_{min} for the best binary and ternary combinations are shown by the blue and red filled symbols in (i). (ii) Corresponding TCC profiles of the best binary and ternary combinations for X7 (-55 to 125 °C) classification

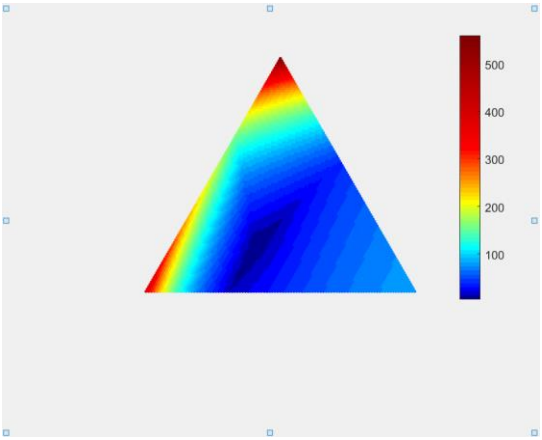

Figure S1 (d). Animated gif of the ternary phase diagram highlighting the location of TCC_{min}